Supplementary Information: Large flux-mediated coupling in hybrid electromechanical system with a transmon qubit

Tanmoy Bera, Sourav Majumder, Sudhir Kumar Sahu, and Vibhor Singh*
Department of Physics, Indian Institute of Science, Bangalore-560012 (India)

Supplementary Note 1. Summary of device parameters

Table S1 lists some important device parameters.

Device parameters		
	Symbol	**Value**
Cavity dimension	$d_x \times d_y \times d_z$	35×35×4 mm^3
Bare cavity frequency	$\omega_c/2\pi$	5.993 GHz
Maximum qubit frequency	$\omega_q^0/2\pi$	7.982 GHz
Qubit-cavity coupling rate	$J/2\pi$	85 MHz
Anharmonicity	$\alpha/2\pi$	-132 MHz
Room temperature junction resistance	R_n	3.67 kΩ
Josephson inductance of SQUID	L_J	4.6 nH
Junction capacitance	C_J	5 fF
Maximum Josephson energy	E_J^0/h	33.4 GHz
Charging energy from black-box simulation	E_C/h	255 MHz
Cavity impedance (simulation)	Z_c	0.6 Ω
Qubit impedance (simulation)	Z_q	275 Ω
SQUID loop area	A	$\sim$ 166 μm^2
Effective SQUID loop width (SQUID area / length of mechanical resonator)	w	$\sim$ 3.33 μm
SiN film thickness	d_1	100 nm
Al coating thickness	d_2	50 nm
Mechanical resonator length	l	$\sim$ 45 μm
Mechanical resonator width	b	300 nm
Mechanical resonator thickness	$d = (d_1 + d_2)$	150 nm
Tensile stress in SiN film	T	$\sim$ 2 GPa
Total mass of the mechanical resonator	m	$\sim$ 5.6 pg
Mechanical resonator frequency	$\omega_m/2\pi$	6.5849 MHz
Maximum applied magnetic field	B_{max}	3.7 mT

TABLE S1: Summary of parameters for the device studied in the main text

Supplementary Note 2. Device Fabrication and measurement setup:

The device is fabricated on a 5×8 mm^2 silicon-(100) substrate coated with 100 nm highly pre-stressed SiN, deposited using LPCVD method. The entire design is patterned in a single electron-beam lithography step using a bilayer resist stack of LOR and PMMA. Subsequently, the shadow evaporation technique is used to deposit aluminum with an intermediate step of oxidation to realize tunnel Josephson junctions. Fig. S1(a) shows the optical image of the device after aluminum deposition.

To pattern the nanowire and release it from the substrate, we use two steps etching procedure. First, the exposed SiN is vertically etched by the reactive ion etching using SF_6 and CHF_3 plasma. The aluminum film naturally acts as a mask layer and thus protects the SiN underneath it. In the second step of etching, a modified TMAH based etchant is used to remove the exposed silicon while providing excellent selectivity against Al and SiN[1,2]. For the etchant we prepare, the etch rate of Si along 100-direction is much faster than the 110- and 111-directions. Following wet-etching, the samples are thoroughly rinsed in DI water and IPA. The samples are then dried using a gentle blow of N_2, without any critical-point drying. After the etch processes, we consistently observe a 30-50% increase in the room-temperature tunnel resistance of the junctions.

The fabricated sample is then placed inside a 3D copper cavity, machined out of OFHC copper (shown in Fig. S1(b)). Subsequently, the cavity assembly is cooled down to 25 mK in a dilution refrigerator. The copper cavity, along with

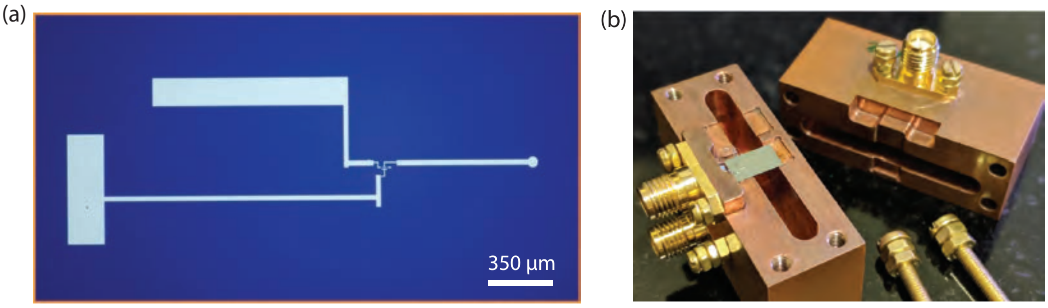

FIG. S1: (a) An optical image of the device before the silicon nitride (SiN) removal. The dark-blue color is due to 100 nm SiN coating over the Si substrate. (b) Image of the device placed in one half of the 3D waveguide cavity while the other half is placed beside. Wirebonds used to realize a single-ended qubit mode can be seen as well. The top SMA-port on the cavity-half showing two connectors is used for mechanical actuation.

a small solenoid, is kept inside a cryoperm-shield to protect from ambient magnetic field fluctuations. Fig. S2 shows the schematic of the complete measurement setup used in the experiment.

Supplementary Note 3. Device design simulation:

We use the black-box circuit quantization (BBQ) technique to simulate the design of the single-ended qubit[3]. We compute the imaginary part of the admittance Y_{sim}, as seen by the Josephson junction, with patterned substrate placed inside. For such computation, a lumped port is defined at the position of SQUID loop. The total reactive admittance, including the SQUID inductance and capacitance, is given by $Y_{\text{total}} = Y_{\text{sim}} + \omega C_J - \frac{1}{\omega L_J}$. Using the junction capacitance C_J= 5 fF and Josephson inductance L_J = 7.5 nH of the SQUID loop, the plot of Y_{total} and Y_{sim} is shown in Fig. S3(a). The zero-crossings with the positive slops in Y_{total} denote the qubit and the cavity mode frequencies. By varying L_J, we identified the crossing on the right as the qubit mode.

The mechanical actuation electrode is designed in a way that the qubit relaxation rate through it can be kept lower, while maintaining sufficient actuation ability to drive the mechanical resonator. Apart from restricting the driveline within the cavity recess, we compute the qubit energy relaxation through the drive port. We simulate the qubit relaxation rate with and without the mechanical actuation electrode. The difference of two relaxation rates k_{leak} as a function of qubit frequency, is shown in Fig. S3(b).

Supplementary Note 4. Estimation of the mechanical resonator frequency:

The mechanical resonator is comprised of a highly pre-stressed (∼2 GPa) SiN beam of thickness 100 nm, with 50 nm coating of aluminum on top. Using Euler-Bernoulli's beam theory[4], the estimated frequency of the mechanical resonator is given by,

$$f_j = \frac{j^2\pi}{2L^2}\sqrt{\frac{(EI)_{eff}}{(\rho A)_{eff}}}\sqrt{1+\frac{(\sigma A)_{eff}L^2}{j^2(EI)_{eff}\pi^2}}$$

where j = 1, 2, 3,... denotes the vibrational mode index, L is the length of nano-beam and $(EI)_{eff}$, $(\sigma A)_{eff}$, and $(\rho A)_{eff}$ are the effective tensile stress, effective bending rigidity, and effective density respectively.

The effective density is given by,

$$(\rho A)_{eff} = \frac{\rho_1 d_1 + \rho_2 d_2}{d_1 + d_2} A = \rho\ A,$$

the effective bending rigidity is given by

$$(\sigma A)_{eff} = \frac{(\sigma_1 d_1 + \sigma_2 d_2)}{d_1 + d_2} A = \sigma\ A,$$

where $A = b\ (d_1 + d_2)$ is the cross sectional area of the mechanical resonator.

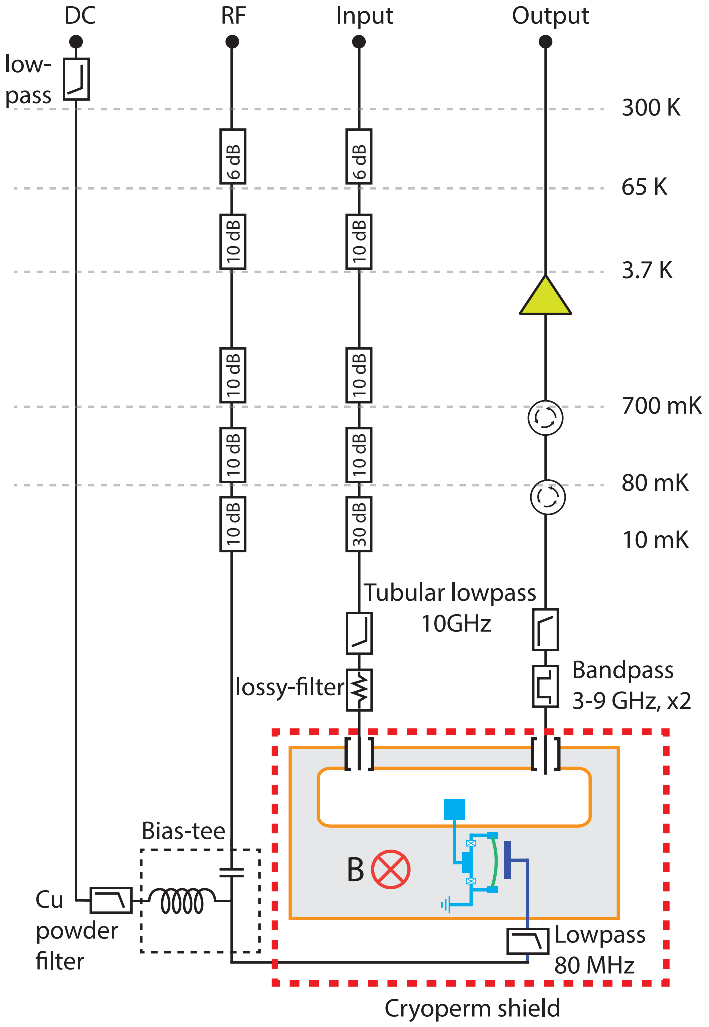

FIG. S2: Schematic of the measurement setup: The input line has 66 dB of cryogenic attenuation, where rf line has 46 dB of fixed attenuation. The bias-tee adds the rf and dc signals, which are used to actuate the mechanical oscillator. The cavity is kept inside a superconducting coil, use to apply the magnetic field B. A cryo-perm shield, shown as a red dashed rectangular box, encloses the sample and superconducting coil setup and provides very effective protection against the magnetic field fluctuations outside the fridge.

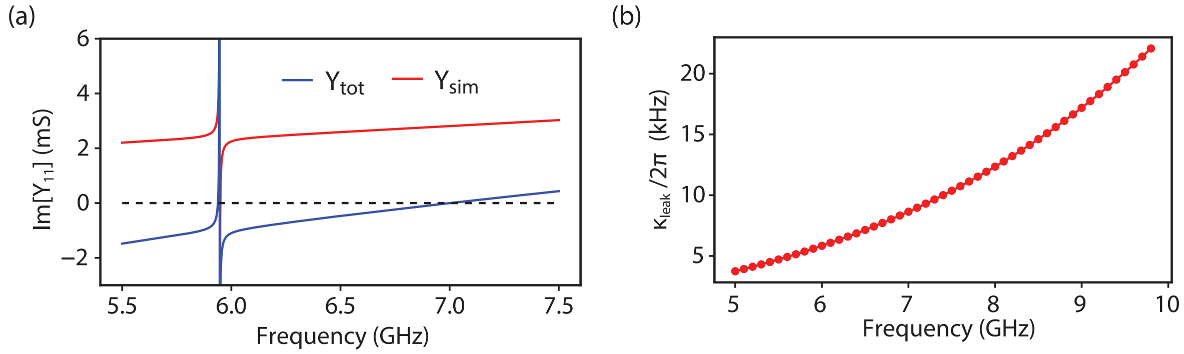

FIG. S3: (a) Admittance of the design computed using a finite element electromagnetic solver. $Y_{\rm sim}$ is the imaginary part of the admittance without the Josephson junction, and $Y_{\rm tot}$ is the imaginary part of the total admittance when the SQUID loop is present. (b) The qubit relaxation rate through the mechanical actuation port is plotted against the qubit frequency.

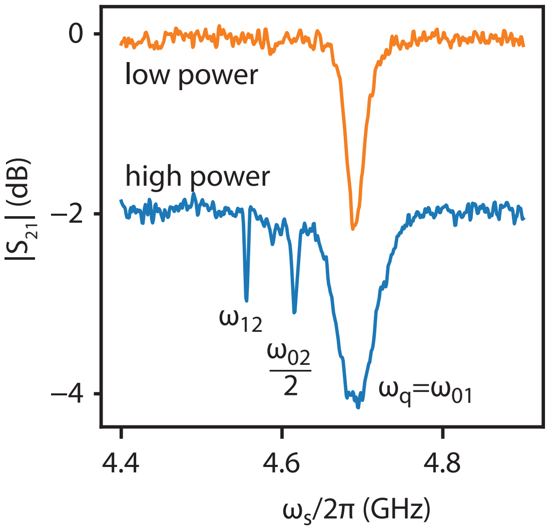

FIG. S4: Two-tone spectroscopy measurement of the qubit for two different spectroscopy powers. At low power, the dip represents the qubit transition from ground to the first excited state. With strong spectroscopy drive, the higher transitions become visible. An offset of -2 dB has been added to the data at the larger drive power to bring clarity.

The effective tensile stress for in-plane and out-of-plane mode is different. For the out-of-plane mode, it is given by

$$(EI)_{eff-oop} = b\frac{E_1^2 d_1^4 + 2E_1E_2d_2(2d_1^3 + 2d_1d_2^2 + 3d_1^2 d_2) + E_2^2 d_2^4}{12(E_1d_1 + E_2d_2)} = E_1 I_{eff}^{oop}.$$

Similarly, for the in-plane mode, it is given by,

$$(EI)_{eff-ip} = \frac{b^3(E_1d_1 + E_2d_2)}{12} = E_1 I_{eff}^{ip},$$

where b denotes the width of the mechanical resonator, d_1 and d_2 are the thickness of SiN and aluminium layers.

We use a Young's modulus of rigidity of $E_1 = 160$ GPa, tensile stress $\sigma_1 = 2$ GPa, and mass density $\rho_1 = 2800$ kg/m^3 for SiN and $E_2 = 69$ GPa, density $\rho_2 = 2700$ kg/m^3 for aluminum. The stress in aluminium film is negligible, and it does not affect the total tensile stress. Effectively, the aluminum coverage over SiN nanobeam increases the mass of the mechanical resonator, which leads to a decrease in the frequency. Using the parameters given above, we estimate the resonant frequency of the fundamental in-plane vibrational mode to be 7.7 MHz.

Supplementary Note 5. Measurement of the qubit anharmonicity:

We use the two-tone spectroscopy technique to measure the qubit anharmonicity. A weak probe near the cavity-frequency is used to continuously monitor transmission through the cavity, while a second spectroscopy tone ω_s near the qubit frequency is swept. When ω_s matches with allowed qubit transitions, the transmission through the cavity changes due to the dispersive coupling.

Fig. S4 shows the two-tone spectroscopy measurements at two different powers of the spectroscopy tone. At larger spectroscopy power, higher transition ω_{12}, and the two-photon transition ω_{02} become visible. We determine the qubit anharmonicity $\alpha \equiv \omega_{12} - \omega_q$ of $-2\pi\times 132$ MHz. It is important to mention that in a traditional 3D-transmon design, the qubit anharmonicity is approximately given by $-E_C$. Due to the modified design used here, the geometrical inductance of the wirebonds L_w dilutes the qubit anharmonicity.

In the limit, SQUID inductance $L_J \gg L_w$, the anharmonicity is given by[5], $\alpha \approx -E_C/(1 + L_w/L_J)^3$. From the room temperature SQUID resistance measurement and finite element simulation of E_C we estimate $L_w \approx 1.13$ nH, and $L_J \approx 4.6$ nH.

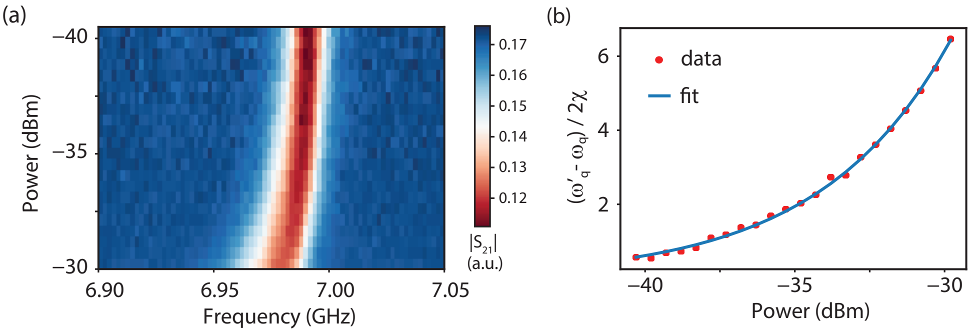

FIG. S5: (a) ac-Stark shift in two-tone spectroscopy: Plot of transmission through the cavity at dressed cavity frequency, while sweeping the spectroscopy frequency near the qubit transition with varying probe power. The red color represents the qubit transition. (b) Normalized qubit frequency shift, proportional to the number of intra-cavity photons, with increasing injected probe power.

Supplementary Note 6. ac-Stark shift and the calibration of the intra-cavity photons:

Fig. S5(a) shows the two-tone spectroscopy measurement when the qubit is dispersively detuned. The qubit transition frequency decreases with increasing probe power due to the photon-induced ac-Stark effect. The shifted qubit frequency is given by $\omega'_q = \omega_q + 2n\chi$, where n is the mean intra-cavity photon number[6]. We detune the qubit by ~ 1 GHz above the cavity mode near 6.992 GHz, and perform the two-tone spectroscopy measurements with varying probe power.

The dispersive shift is given by $\chi = J^2 \frac{\alpha}{\Delta(\Delta+\alpha)}$, where J is the coupling strength between the qubit and the cavity mode, α is the anharmonicity, and $\Delta = \omega_q - \omega_c$ is the qubit detuning. From the independent measurements of anharmonicity and qubit-cavity coupling, we compute the dispersive shift. The dispersive shift calculated this way, is then used to calibrate the number of intra-cavity photons.

The experimentally extracted intra-cavity photon number with increasing probe power from the signal generator, is plotted in Fig. S5(b). This allows us to estimate the total microwave attenuation of the input line (from the microwave signal generator to the input port of the cavity), estimated to be 79.7 dB.

Supplementary Note 7. Thermal motion and mechanical mode temperature calibration:

To determine the thermal occupation of the mechanical resonator, we operate the system at $\omega_+/2\pi = 6.025$ GHz. While pumping this mode with a cw-tone at 6.025 GHz, we measure the total integrated power P_m in lower sideband. Also, the transmitted power P_d at the carrier frequency ω_+ is recorded. To eliminate the records made during any flux-jump event, we record the transmission $|S_{21}|$ before and after every trace measured by the spectrum analyzer. While we take this precaution, it is worth pointing out that all the data shown in the main manuscript is from the measurements runs, where we did not observe any flux-jump. Fig. S6(a) shows a 2D color-map of 200 traces of the power spectral density (PSD) measured with a spectrum analyzer. A plot of $|S_{21}|$ (at ω_+) for all the 200 traces is shown in Fig. S6(b).

Fig. S6(c) and (d) show the average trace of lower-sideband noise spectra measured at 25 mK and 50 mK, respectively. The down-converted power at the lower sideband frequency for zero detuning driving is given by $P_m = P_d \left(g_+/(\kappa^2/4 + \omega_m^2)\right) n_m^{th}$.

Device parameter	$T = 25$ mK	$T = 50$ mK
Transmitted power at carrier frequency P_d	-75.9 dBm	-77.3 dBm
Cavity dissipation rate $\kappa/2\pi$	4.1 MHz	5.1 MHz

TABLE S2: System parameters used for the calibration of phonon occupancy

Assuming the vacuum coupling rate to be the same for two temperatures, from the results shown in Fig. S6(c), (d) and the parameter values in Table S2, we find the ratio $n_m^{25}/n_m^{50} \approx 1$. This led us to conclude that the mechanical resonator is thermalized to 50 mK or a higher temperature. The vacuum coupling rate, shown in Fig. 3(c) of the

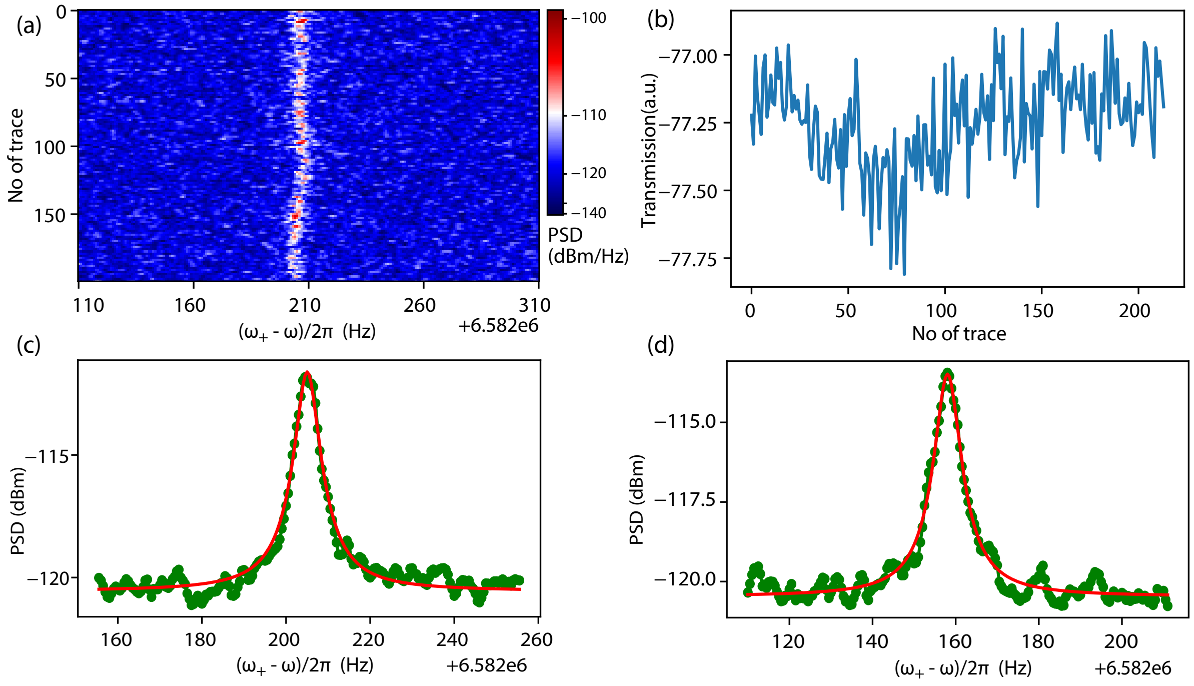

FIG. S6: (a) A color plot of 200 power spectral density traces. (b) Cavity transmission $|S_{21}(\omega_+)|$ during the measurement shown in (a). The transmission value is checked before initiating the PSD trace and validated after the PSD trace is over. (c) and (d) show the average power spectral density at the lower sideband measured at 25 and 50 mK, respectively. The dressed mode is driven with a mean photon occupation of 0.2 at 6.025 GHz.

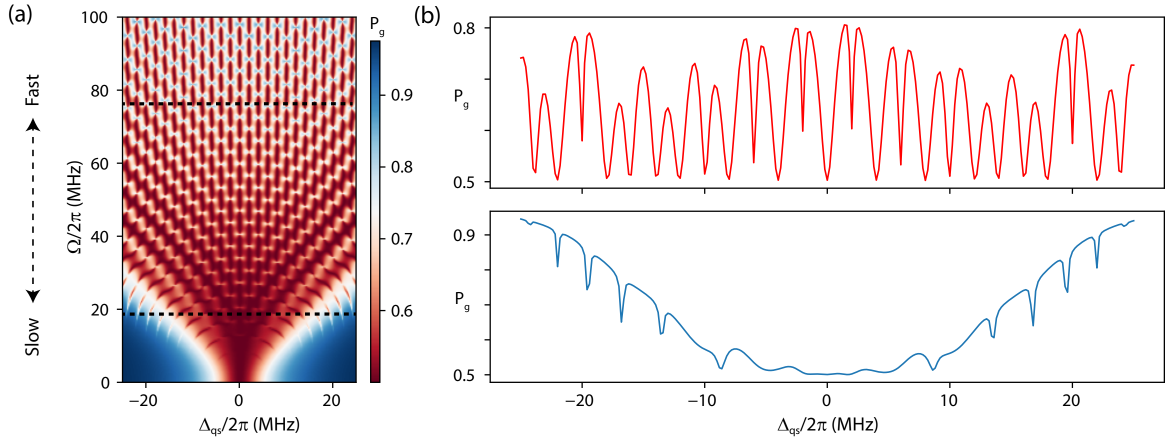

FIG. S7: (a) The LZS interference pattern with increasing qubit frequency deviation. The time-averaged value of $P_g = (1 - \langle\hat{\sigma}_z\rangle)/2$ is plotted with respect to detuning Δ_{qs}. (b) The top (bottom) plot shows the response for high (low) values of qubit frequency deviation. The linecuts are taken at $\Omega/2\pi = 76$ MHz (top) and 18 MHz (bottom), indicated by the black dashed line in the color plot. The calculations were done using $\Omega_R/2\pi = 8$ MHz, $\omega_m/2\pi = 2$ MHz and $\gamma_1/2\pi = 0.1$ MHz.

main text, has been calculated assuming a thermalization to 53 mK as these values fall roughly on the estimated values of g_+ from the device parameters.

Supplementary Note 8. Theoretical Model to understand Landau-Zener-Stückelberg (LSZ) interference:

When the qubit is detuned far away from the cavity, the total Hamiltonian of the system can be written as[6],

$$H^{dis} = \hbar\omega_c \hat{a}^\dagger \hat{a} + \frac{\hbar\omega_q}{2}\hat{\sigma}_z + \hbar\omega_m \hat{b}^\dagger \hat{b} + \hbar\chi\hat{\sigma}_z \hat{a}^\dagger \hat{a} + \hbar g_{qm}\hat{\sigma}_z(\hat{b} + \hat{b}^\dagger) \tag{S1}$$

Due to a large difference between the qubit and mechanical resonator frequency, and g_{qm} being much smaller than the qubit frequency, we invoke the adiabatic approximation. A coherent drive on the mechanical resonator effectively results in a frequency-modulated qubit. The effective Hamiltonian can be written as,

$$H = \hbar\omega_c \hat{a}^\dagger \hat{a} + \frac{\hbar(\omega_q + \Omega\sin(\omega_m t))}{2}\hat{\sigma}_z + \hbar\omega_m \hat{b}^\dagger \hat{b} + \hbar\chi\hat{\sigma}_z \hat{a}^\dagger \hat{a} \tag{S2}$$

where $\Omega = g_{qm}\epsilon_m/x_{zp}$ is the qubit frequency deviation, and ϵ_m is the mechanical amplitude. Due to the longitudinal coupling, the mechanical resonator only contributes to the modulation of the qubit frequency.

To simulate the two-tone spectroscopy data (main text Fig.4), we add probe and spectroscopy drives to the Hamiltonian. After performing the rotating frame transformation at the spectroscopy frequency ω_s and the probe frequency, we get an effective Hamiltonian given by,

$$H = \frac{\hbar(\Delta_{qs} + \Omega\sin(\omega_m t))}{2}\hat{\sigma}_z + \hbar\chi(1 + \hat{\sigma}_z)\hat{a}^\dagger \hat{a} + \epsilon_{probe}(\hat{a} + \hat{a}^\dagger) + \frac{\Omega_R}{2}\hat{\sigma}_x, \tag{S3}$$

where $\Delta_{qs} = \omega_q - \omega_s$, ϵ_{probe} is the amplitude of the probe signal, and Ω_R is the amplitude of the spectroscopy signal (the Rabi-flop rate).

The time evolution of different operators can be calculated by using the master equation solver of the QuTip package[7]. We solve for the steady-state of $\langle\hat{a}\rangle_{ss}$ using the total Hamiltonian and define the transmission as the ratio of the time-averaged value of $\langle\hat{a}\rangle_{ss}$ to the probe amplitude *i.e.* $S_{21} = \overline{\langle\hat{a}\rangle_{ss}}/\epsilon_{probe}$. Spectroscopy signal was varied near the qubit transition, while the probe signal frequency was kept fixed at the dressed cavity frequency corresponding to the qubit being in the ground state. Their amplitudes were kept constant during simulation *i.e.* $\Omega_R/2\pi = 3$ MHz and $\epsilon_{probe}/2\pi = 10$ kHz. We use a dispersive shift $\chi/2\pi = -0.71$ MHz. The results from such calculations are plotted as the solid lines in Fig. 4(b) of the main text.

In the two-tone spectroscopy measurements, the measured signal is directly related to $\langle\hat{\sigma}_z\rangle$. Therefore, the spectrum can also be worked out using the Hamiltonian of the qubit subspace only. The model, therefore, can be simplified to a two-level system (TLS), which is driven along the longitudinal direction (by the mechanical motion) and along the transverse direction (by the spectroscopy tone) simultaneously. In a frame rotating at the spectroscopy frequency, the Hamiltonian can be written as,

$$H_{TLS} = \frac{\Delta_{qs} + \Omega\sin(\omega_m t)}{2}\hat{\sigma}_z + \frac{\Omega_R}{2}\hat{\sigma}_x\ . \tag{S4}$$

The time evolution of the system can be worked out by using the Lindblad master equation,

$$\dot{\rho} = -\frac{i}{\hbar}[H_{TLS}, \rho] + \gamma_1 \mathcal{D}[\hat{\sigma}_-]\rho + \frac{\gamma_\phi}{2}\mathcal{D}[\hat{\sigma}_z]\rho, \tag{S5}$$

where γ_1 and γ_ϕ are the qubit relaxation and the qubit pure dephasing rates, respectively and the Lindblad superoperator $\mathcal{D}[\hat{F}]$ is defined as,

$$\mathcal{D}[\hat{F}]\rho = \hat{F}\rho\hat{F}^\dagger - \frac{1}{2}\hat{F}^\dagger\hat{F}\rho - \frac{1}{2}\rho\hat{F}^\dagger\hat{F}. \tag{S6}$$

This leads to a set of equation of motion as:

$$\frac{d}{dt}\langle\hat{\sigma}_x\rangle = -(\Delta_{qs} + \Omega\sin(\omega_m t))\langle\hat{\sigma}_y\rangle - (\frac{\gamma_1}{2} + \gamma_\phi)\langle\hat{\sigma}_x\rangle \tag{S7a}$$

$$\frac{d}{dt}\langle\hat{\sigma}_y\rangle = -\Omega_R\langle\hat{\sigma}_z\rangle + (\Delta_{qs} + \Omega\sin(\omega_m t))\langle\hat{\sigma}_x\rangle - (\frac{\gamma_1}{2} + \gamma_\phi)\langle\hat{\sigma}_y\rangle \tag{S7b}$$

$$\frac{d}{dt}\langle\hat{\sigma}_z\rangle = \Omega_R\langle\hat{\sigma}_y\rangle - \gamma_1(1+\langle\hat{\sigma}_z\rangle) \tag{S7c}$$

We compute the steady-state value of $\langle\hat{\sigma}_z\rangle$ by numerically integrating the Equation S7. To replicate the measurements, we vary the spectroscopy frequency near the ω_q (Δ_{qs}) and strength of the modulation Ω and plot the steady state value of $(1-\langle\hat{\sigma}_z\rangle)/2$.

Fig. S7 shows the result from the numerical calculations showing the characteristic Landau-Zener-Stückelberg (LZS) interference pattern[8]. In the limit of fast-passage across the avoided crossing ($\Omega_R \ll \Omega\omega_m/\Omega_R$), the interference fringes are separated by the modulation frequency ω_m. In the slow-passage limit ($\Omega_R \gtrsim \Omega\omega_m/\Omega_R$), as the system undergoes the avoided crossing, the probability of diabatic transition increases, and the separation between the fringes is no longer solely determined by ω_m.

Splitting of the qubit spectrum can also be understand from a semi-classical model. In this approach, we calculate the time averaged value of $\langle\hat{\sigma}_z\rangle$ when qubit frequency is being modulated at ω_m, thereby asserting that adiabatic approximation.

Using Eq. S7, the steady state value of $\langle\hat{\sigma}_z\rangle$ can be obtained as

$$\langle\hat{\sigma}_z\rangle = -1 + \frac{\Omega_R^2\frac{\gamma_2}{\gamma_1}}{\gamma_2^2 + \Omega_R^2\frac{\gamma_2}{\gamma_1} + [\Delta_{qs} + \Omega\sin(\omega_m t)]^2}, \tag{S8}$$

where $\gamma_2 = \left(\frac{\gamma_1}{2} + \gamma_\phi\right)$. We define the time averaged value of $\langle\hat{\sigma}_z\rangle$ as,

$$\overline{\langle\hat{\sigma}_z\rangle} = \frac{1}{T}\int_0^T \langle\hat{\sigma}_z\rangle\, dt, \tag{S9}$$

where $T = 2\pi/\omega_m$ is the time period of the mechanical oscillation. Therefore,

$$\overline{\langle\hat{\sigma}_z\rangle} = -1 + \frac{\Omega_R^2}{T}\frac{\gamma_2}{\gamma_1}\int_0^T \frac{dt}{\gamma_2^2 + \Omega_R^2\frac{\gamma_2}{\gamma_1} + [\Delta_{qs} + \Omega\sin(\frac{2\pi t}{T})]^2}. \tag{S10}$$

To carry out the integral, we first scale the time variable and then recast the integral as,

$$\overline{\langle\hat{\sigma}_z\rangle} = -1 - \frac{\Omega_R^2\frac{\gamma_2}{\gamma_1}}{2\pi\sqrt{\gamma_2^2 + \Omega_R^2\frac{\gamma_2}{\gamma_1}}}\,\mathrm{Im}\left[\int_0^{2\pi} \frac{dx}{i\,\sqrt{\gamma_2^2 + \Omega_R^2\frac{\gamma_2}{\gamma_1}} + \Delta_{qs} + \Omega\sin(x)}\right] \tag{S11}$$

This integral can be transformed into a function of a complex variable and solved using Cauchy's integral formula with a contour described by $|z| = 1$. The important part of the calculation is the fact that for any value of Δ_{qs}, there is only one pole that exists inside the contour. Using the residue theorem, the final answer can be written as,

$$\overline{\langle\hat{\sigma}_z\rangle} = -1 + \frac{\Omega_R^2}{\beta}\frac{\gamma_2}{\gamma_1}\left|\sin\left(\frac{\theta}{2}\right)\right|, \tag{S12}$$

$$\beta = \sqrt{\gamma_2^2 + \Omega_R^2\frac{\gamma_2}{\gamma_1}}\;\sqrt[4]{\left(\Delta_{qs}^2 - \gamma_2^2 - \Omega_R^2\frac{\gamma_2}{\gamma_1} - \Omega^2\right)^2 + 4\Delta_{qs}^2\left(\gamma_2^2 + \Omega_R^2\frac{\gamma_2}{\gamma_1}\right)} \tag{S13}$$

and

$$\theta = \tan^{-1}\left[\frac{2\Delta_{qs}\sqrt{\gamma_2^2 + \Omega_R^2\frac{\gamma_2}{\gamma_1}}}{\Delta_{qs}^2 - \gamma_2^2 - \Omega_R^2\frac{\gamma_2}{\gamma_1} - \Omega^2}\right] \tag{S14}$$

Using the decoupled cavity-Bloch equation in the steady state, the normalized transmission through the cavity can be written as,

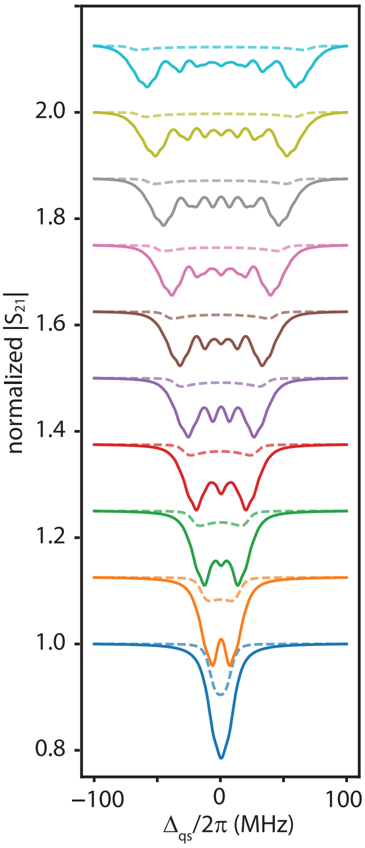

FIG. S8: The solid lines show the results from the Master equation. The dotted lines show the results from semi-classical calculation. Clearly the calculations performed using the Master equation matches the experimental results better. The calculations were done using the same parameters as used for Fig-4 shown in the main text.

$$S_{21} = \frac{-i\kappa/2}{\kappa/2 + i\chi\left(1 + \overline{\langle\hat{\sigma}_z\rangle}\right)} \tag{S15}$$

Figure S8 shows the qubit spectrum using Eq. S15. For comparison, solution obtained from the Master equation have been included as well.

---

[*] Electronic address: v.singh@iisc.ac.in

[1] Yan, G., Chan, P. C. H., Hsing, I.-M., Sharma, R. K., Sin, J. K. O., and Wang, Y. *Sensors and Actuators A: Physical* **89**(1), 135–141 March (2001).

[2] Norte, R. A. *Nanofabrication for On-Chip Optical Levitation, Atom-Trapping, and Superconducting Quantum Circuits.* phd, California Institute of Technology, (2015).

[3] Nigg, S. E., Paik, H., Vlastakis, B., Kirchmair, G., Shankar, S., Frunzio, L., Devoret, M. H., Schoelkopf, R. J., and Girvin, S. M. *Physical Review Letters* **108**(24), 240502 June (2012).

[4] Seitner, M. J., Gajo, K., and Weig, E. M. *Applied Physics Letters* **105**(21), 213101 November (2014).

[5] Chen, Y., Neill, C., Roushan, P., Leung, N., Fang, M., Barends, R., Kelly, J., Campbell, B., Chen, Z., Chiaro, B., Dunsworth, A., Jeffrey, E., Megrant, A., Mutus, J., O'Malley, P., Quintana, C., Sank, D., Vainsencher, A., Wenner, J., White, T., Geller, M. R., Cleland, A., and Martinis, J. M. *Physical Review Letters* **113**(22), 220502 November (2014).

[6] Koch, J., Yu, T. M., Gambetta, J., Houck, A. A., Schuster, D. I., Majer, J., Blais, A., Devoret, M. H., Girvin, S. M., and Schoelkopf, R. J. *Physical Review A* **76**(4), 042319 October (2007).

[7] Johansson, J. R., Nation, P. D., and Nori, F. *Computer Physics Communications* **183**(8), 1760–1772 August (2012).

[8] Shevchenko, S. N., Ashhab, S., and Nori, F. *Physics Reports* **492**(1), 1–30 July (2010).